Direct Observation of Oxide Ion Dynamics in $La_2Mo_2O_9$ on the Nanosecond Timescale

Joseph R. Peet [a, b], Chloe A. Fuller [a, b], Bernhard Frick [b], Mohamed Zbiri [b], Andrea Piovano [b], Mark R. Johnson [b] and Ivana Radosavljevic Evans [a*]

[a] Durham University, Department of Chemistry, Science Site, South Road, Durham, DH1 3LE, UK

[b] Institut Laue Langevin, Grenoble, France

ABSTRACT: Quasielastic neutron scattering (QENS), underpinned by ab-initio molecular dynamics (AIMD) simulations, has been used to directly observe oxide ion dynamics in solid electrolyte $La_2Mo_2O_9$ on the nanosecond timescale, the longest timescale probed in oxide ion conductors by neutron scattering to date. QENS gives the activation energy of 0.61(5) eV for this process, while AIMD simulations reveal that the exchange processes, which ultimately lead to long-range oxide ion diffusion in $La_2Mo_2O_9$, rely on the flexibility of the coordination environment around Mo^{6+}, with oxide ions jumps occurring between vacant sites both within and between Mo coordination spheres. Simulations also differentiate between the crystallographic sites which participate in the oxide ion exchange processes, offering the first atomic-level understanding of the oxide ion dynamics in $La_2Mo_2O_9$, which is consistent with the macroscopic experimental observations on this material.

Introduction

Oxide ion conductors are of considerable interest due to their range of environmentally and energy-related applications including oxygen sensors, pumps, separation membranes and solid oxide fuel cells (SOFCs). Understanding the structural characteristics and resulting conduction pathways in these materials is a key requirement in improving their properties through smart design.

One material that has been the subject of much research interest is $La_2Mo_2O_9$, whose oxide ion conducting properties were first reported by Lacorre *et al.*[1] The conductivity reaches 6×10^{-2} S cm^{-1} at 800 °C after an abrupt increase of two orders of magnitude ~550 °C, accompanying a phase transition from the low temperature α-form to the high temperature β-form. The average structure of the high temperature β-$La_2Mo_2O_9$ is cubic, with space group $P2_13$ and a cell parameter a = 7.20 Å.[2] It contains a single unique Mo site and three unique O sites.[3] The room temperature α-structure was found to be a complex superstructure with unit cell dimensions of ~ $2a \times 3a \times 4a$ relative to β-$La_2Mo_2O_9$ and a very small monoclinic distortion.[4] The oxygen atoms in this phase are distributed over 216 unique sites making up 4-, 5- and 6-coordinate MoO_x polyhedra (Figure 1, left). The β-structure represents a time and space average of the α-form, and the α-to-β structural phase transition corresponds to an order-disorder transition which results in the increased mobility of the oxide ions in the material (Figure 1, right); this relationship was subsequently confirmed by a neutron total scattering study.[5] The relationship between the two forms of $La_2Mo_2O_9$ suggests that the oxide ions from all unique crystallographic sites participate in the conduction process in the highly conducting high-temperature form[4] , as had been implied by the low frequency internal friction measurements.[6]

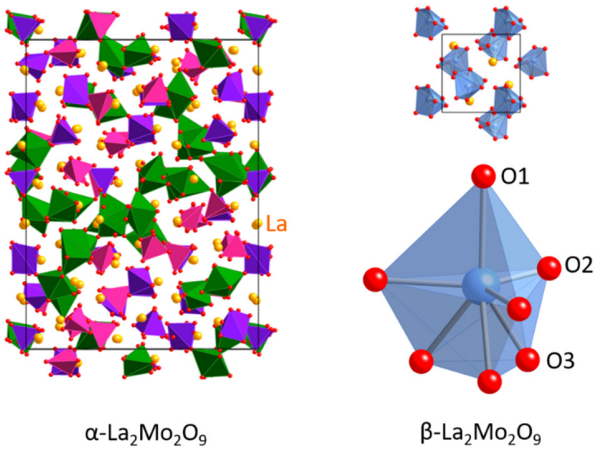

Figure 1. (Left) the room temperature structure of α-$La_2Mo_2O_9$ emphasising different MoO_x coordination polyedra; (Right) structure of β-$La_2Mo_2O_9$ and disordered coordination environment around each Mo.

Research into $La_2Mo_2O_9$ and related materials has largely been focused on trying eliminate the abrupt structural phase transition and stabilise the highly conducting β-form at lower temperatures. This has been attempted by doping with a large number of different cations including

alkali metals[7-9], alkali earths[9, 10], rare earths[3, 11-16], Bi[17-19] and Pb[20] on the La site and transition metals[9, 10, 13, 16, 21, 22] and S[9] on the Mo site. In many cases this has been successful, leading to higher conductivity at lower temperatures than in the parent material. In addition, the phase transition has been shown to be suppressed in $La_2Mo_2O_9$ nanowires which also show extremely high conductivity.[23] These successes have led to further investigation of the utility of these materials in SOFCs as both the electrolyte[24-26] and the anode.[27-29]

Investigation into the precise mechanisms of conduction in $La_2Mo_2O_9$, on the other hand, has been relatively sparse. Initially it was assumed that the partially occupied O2 and O3 sites were the cause of conductivity, with the O1 sites remaining static.[9] It was also observed that doped compounds that maintain the β-phase at low temperature exhibit a change from Arrhenius to Vogel-Fulcher-Tammann (VFT) behaviour at higher temperatures.[3] A study by Corbel *et al.*[30] proposed that the cause of the increasing conductivity was expansion of the faces of the oxygen-centred $O1La_3Mo$ tetrahedral units, allowing the O1 atoms thought to be static to leave their site and diffuse to partially occupied sites on adjacent Mo atoms. This extra conduction path was therefore proposed to be the origin of the VFT behaviour. However, this study was carried out on a Bi-doped sample rather than the parent compound. An *ab initio* molecular dynamics (AIMD) study of $La_2Mo_2O_9$ by Hou *et al.*[31] also found that O1 atoms were involved in oxygen diffusion, being a part of one of the two diffusion paths found. Their study involved only a small simulation box consisting of a single β-unit cell and did not investigate explicitly how the mechanisms changed with temperature. Recently, Kezionis *et al.*[32] reported an analysis based on a distribution of relaxation times using broadband impedance spectroscopy. They observed two relaxation processes in $La_2Mo_2O_9$; one process which is present in both low- and high- temperature phases, although reaching a maximum around the phase transition, and a different process which dominates in the β-phase. They proposed that the reason for the continued presence of the first process in the high temperature phase could be due to it being a part of the other process.

To provide proper atomic-level insight into oxide ion dynamics in $La_2Mo_2O_9$ we have used a combination of quasielastic neutron scattering (QENS) and density functional theory (DFT) calculations. QENS is a technique well suited to studying diffusion phenomena in solids.[33] It enables the determination of, on one hand, the overall diffusion coefficient and, on the other, the study of the single elementary atomic jump process. So far, numerous interesting studies have been carried out on the diffusion of hydrogen in metals,[34] in intercalation compounds,[35] and in solid state proton conductors[36,37]. Despite the ability of QENS to directly observe microscopic oxygen diffusion dynamics, study of oxide ion conductors using this technique has so far only been reported in a few studies, and on timescales of picoseconds[37-39] to hundreds of picoseconds.[40, 41]

In this paper we present the first quasielastic neutron scattering (QENS) study of oxide ion dynamics on a nanosecond timescale, investigating diffusion processes in the fast ion conductor $La_2Mo_2O_9$. We also present the findings from an in depth ab-initio molecular dynamics (AIMD) investigation into $La_2Mo_2O_9$, with a larger simulation box and significantly longer simulation time than that previously reported. From this combination of experimental and computational approaches, we provide new atomic-level insight into the conduction processes occurring in this material.

Experimental

Synthesis of samples for IN16b and IN6 experiments

Samples of $La_2Mo_2O_9$ were prepared from stoichiometric amounts of La_2O_3 and MoO_3. The reactants were thoroughly mixed and ground together then placed in an alumina crucible and fired at 900 ˚C for 72 hours with intermediate grinding and heating and cooling rates of 5 ˚C min^{-1}. Sample purity was confirmed by laboratory powder X-ray diffraction (PXRD).

X-ray Diffraction

Variable temperature X-ray diffraction (VT XRD) experiments were carried out on a Bruker AXS D8 Advance diffractometer with a Vantec detector, Cu K_{α_1} radiation, and an Anton Paar HTK1200 high-temperature attachment and a Vantec detector. The VT XRD data for the extraction of the unit cell parameters of $La_2Mo_2O_9$ were recorded over a 2θ range of 10-120° on heating and cooling between room temperature and 800 °C with a temperature increment of 10 °C and with a collection time of 15 minutes at each temperature. A small amount of Al_2O_3 was used an as internal standard. All data were analysed by Rietveld fitting[42] using TOPAS Academic.[43] The data in the entire temperature range were fitted using the monoclinic structural model, by varying the unit cell parameters and three isotropic temperature factors (one each for La, Mo and O).

Quasielastic and Inelastic Neutron Scattering

Neutron scattering data probing picosecond timescales were collected on time-of-flight spectrometer IN6 at the Institut Laue Langevin (ILL) with an incident neutron wavelength of 5.92 Å. Data were collected at 200 °C and from 500-900 °C in steps of 100 °C. At each temperature data were collected for 8 hours. Data were also collected on a vanadium sample at 20 °C for 6 hours to provide the instrument resolution function.

Neutron scattering data probing nanosecond timescales were collected on the backscattering spectrometer IN16b at the ILL. A 10 g powdered sample was placed in a cylindrical Nb sample holder and exposed to neutrons with an incident wavelength of 6.27 Å. Initially measurements of elastic intensity were made from 450-900 °C with a heating rate of 1/110 °C s^{-1}. Data points were counted every 60 seconds. After confirming the onset of dynamics occurring at

560 °C, QENS measurements were performed at eight temperatures between 550 °C and 750 °C with an energy transfer window of ±10 μeV. Data were collected for 3 hours at each temperature except at 570 °C, just after the onset of dynamics, for which a total of 6 hours of data were collected. For the analysis of QENS data, a resolution function was determined from low temperature data from the sample and a standard vanadium sample – the resolution full-width at half-maximum was 0.73 μeV. The data from both the IN6 and IN16b neutron scattering experiments were analysed using the LAMP software.[44]

Computational

Ab-initio molecular dynamics (AIMD) calculations were carried out using the DFT method implemented in the VASP code.[45] The simulations were performed on a 2 × 2 × 2 supercell of the cubic high temperature $P2_13$ structure[2] giving a simulation box containing 32 La, 32 Mo and 144 O atoms, the largest computationally feasible on a realistic time scale. The O2 and O3 locations were chosen using a random number generator from the partially occupied sites in the high temperature structure in order to match the required stoichiometry and site occupancies. Note that the 500°C AIMD calculation does not refer to the larger 2 × 3 × 4 monoclinic cell which describes the long-range average structure at this temperature. The same simulation box used for all simulations for consistency, however, is representative of the local structure of the material in this entire temperature range, as demonstrated by PDF analysis based on neutron total scattering data.[5] In light of this, the 500°C AIMD simulation is only proposed as a baseline for the dynamics of highly-conductive cubic form of $La_2Mo_2O_9$ stable at higher temperatures. PAW pseudopotentials[46] were used with GGA-PBE functionals.[47] The electronic structure was sampled only at the gamma point. The AIMD calculations were performed at 500 °C, 800 °C, 900 °C and 1000 °C in the NVT ensemble. For the 500 °C and 1000 °C simulations 3.25 × 10^5 steps of 2 fs were calculated giving a total of 650 ps of simulation time. For the 800 °C and 900 °C temperatures 50,000 steps were calculated giving 100 ps of simulation time. Mean square displacements and density of states were produced using the MDANSE code[48] and cloud plots for trajectory visualisation were produced using LAMP.[44] A phonon density of states (DOS) was also determined from gamma-point phonons using DFT with the finite displacement method. This calculation was performed on a slightly smaller 2 × 2 × 1 supercell, produced in the same way as the 2 × 2 × 2 supercell described above, but for which the calculation time was ten times shorter.

Results and Discussion

Probing Dynamics on the Picosecond Timescale

Figure 2 shows the inelastic neutron scattering data collected on IN6. The variation of the angle-integrated scattering function, $S(\omega)$, with temperature shows inelastic contributions that increase in amplitude with increasing temperature. This increase can be accounted for at all temperatures by the phonon Bose population factor, and therefore there is no quasielastic signal. The oxygen diffusion dynamics in $La_2Mo_2O_9$ are therefore slower than the picosecond timescales probed by IN6 and previously observed in $Bi_{26}Mo_{10}O_{69}$[38] and $Sr_2Fe_2O_5$.[39]

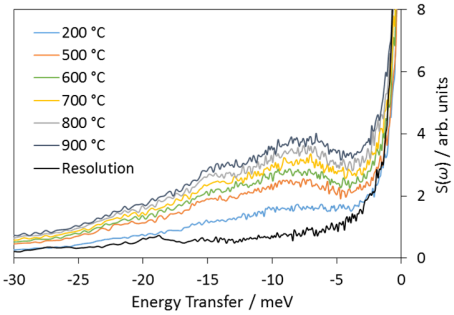

Figure 2. The *Q*-integrated scattering function, S(ω), against neutron energy transfer at various temperatures for a sample of $La_2Mo_2O_9$ measured on IN6. A resolution function from a vanadium sample has been provided for comparison.

Figure 3a shows the density of states measured on IN6 at 900 °C compared with the density of states calculated from complementary AIMD simulations at 1000 °C and DFT phonon calculations. All three curves match closely, with the two main peaks located at 20 and 40 meV clearly present in all three cases. The two calculated DOS curves both have a third peak at 100 meV, whereas the experimental DOS is not so clear at high energies since the high energy phonons are weakly populated at the temperature of the measurement and the Bose population factor is applied to a weak signal.

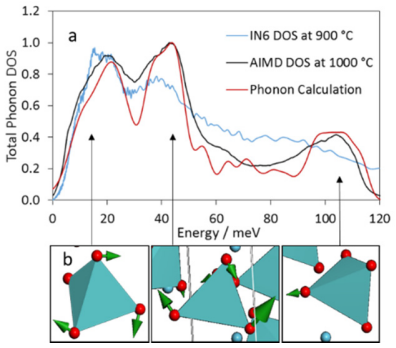

Figure 3. a) Phonon DOS calculated from AIMD and DFT phonon calculations compared with experimental results from IN6 neutron scattering. The calculated curves have been weighted according to neutron scattering power of La, Mo and O and all three curves have been scaled to reach a maximum value of 1. **b)** Types of modes associated with the three main peaks in the DOS. The green arrows represent simultaneous atom movement with the size scaled to the distance moved. Red atoms are O and blue atoms and polyhedra are Mo.

The agreement between the three methods of determining the DOS supports the validity of our AIMD simulations and provides evidence that conclusions drawn from them are reliable. The locations of the peaks are consistent with those found in similar oxide ion conducting materials such as $Bi_{26}Mo_{10}O_{69}$.[38] The phonon calculations allow the identification of the types of modes that make up each part of the DOS. The lowest energy modes found in the first peak are librations of the Mo-O polyhedra; the second peak is made up of bending modes involving distortions of the polyhedra. These give way to stretching modes found in the high energy band. Representative examples of these motions can be seen in figure 3b.

Probing Dynamics on the Nanosecond Timescale

A plot of elastic intensity against temperature for $La_2Mo_2O_9$ is shown in figure 4. There is a large decrease of around 30 % in the elastic intensity around 560 °C, deviating from the gradual decrease in intensity due to Debye-Waller effects observed elsewhere in the temperature range. This coincides with the α-to-β phase transition, as demonstrated by the unit cell volume dependence on temperature shown in figure S1.

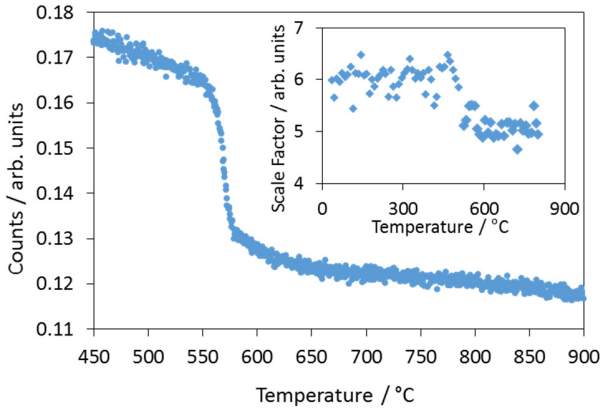

Figure 4. A plot of the elastic intensity against temperature for a neutron scattering experiment on La2Mo2O9 carried out with IN16b. Each temperature point was collected for 60 seconds. Inset: The temperature dependence of the $La_2Mo_2O_9$ scale factor from Rietveld refinements normalised to an Al_2O_3 internal standard.

An abrupt decrease of Bragg intensity (beyond that due to the Debye-Waller factor) can also be observed in the plot of the variation of the $La_2Mo_2O_9$ scale factor from Rietveld refinements against the VT XRD data (figure 4, inset), demonstrating the use of laboratory XRD data as a preliminary screening method for potential neutron scattering experiments. The scale factor shown is normalised relative to that of an Al_2O_3 internal standard (in which no phase transition occurs). The observed decrease is around 15 %, lower in magnitude than that seen in the neutron elastic data, mainly due to the relative scattering power of oxygen to La and Mo being much lower for X-rays than neutrons.

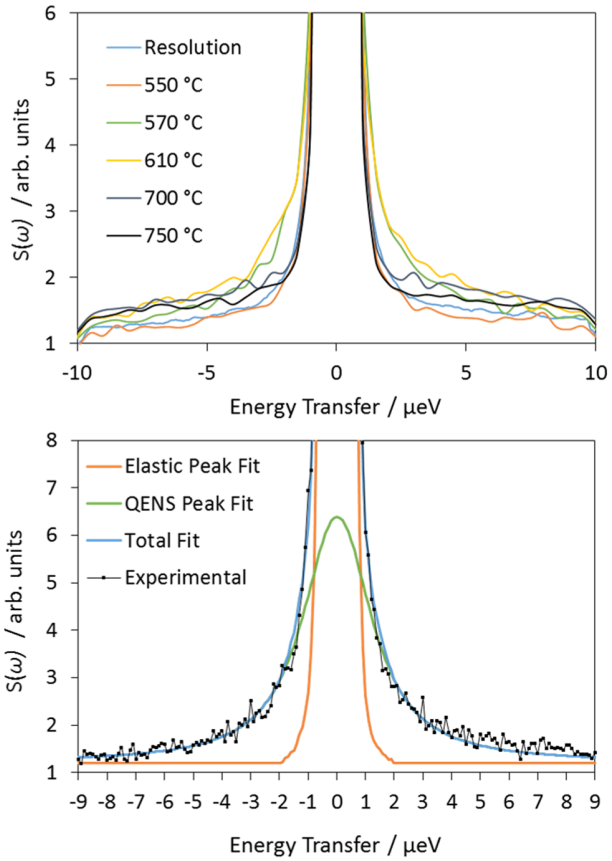

Figure 5. a) $S(\omega)$ spectra for inelastic neutron scattering measurements on $La_2Mo_2O_9$ at various temperatures with a maximum energy transfer of ±10 μeV. The data has been summed over all Q. A resolution function is also shown. **b)** Fitting of the 570 °C dataset.

The phase transition leads to higher conductivity and indicates the onset of oxygen dynamics on the nanosecond timescales probed by IN16b. These data represent the first direct observation of oxygen dynamics via neutron scattering on these timescales which are the longest reported to date.

Plots of $S(\omega)$ against energy transfer, figure 5a, for a selection of the measured temperatures show an elastic peak as well as a clear quasielastic signal above 550 °C that evolves with temperature. No QENS signal is observed in the 550 °C data set, which is similar to the resolution function in terms of linewidth. At 570 °C and above the QENS signal is very clear, with broadening becoming visually apparent at 610 °C. This broadening becomes very large at high temperatures with the amplitude of the QENS peak therefore becoming very low at 750 °C. This broadening is due to the continued increase in the rate of motion as temperature increases, and the evolution of the full width at

half maximum (FWHM) of the peak can be used to determine an activation energy for the dynamic process. To do this, the QENS features at each temperature were fitted with a delta function representing the elastic peak and a Lorentzian for the quasielastic peak, both convoluted with the resolution function as shown in figure 5b. A flat background was used in the fitting. The very large broadening at 750 °C made a reliable fit impossible due to the Lorentzian linewidth being larger than the measured energy transfer window. Assuming a Chudley-Elliott jump diffusion model the linewidths Γ obtained from these fits are proportional to the diffusion coefficients and so can be expected to follow an Arrhenius relationship with temperature.[49] A plot of $\ln(\Gamma)$ against $1000/T$ (figure 6) yields an activation energy of 0.61(5) eV. This is in very good agreement with the value of 0.66(9) eV found by Liu *et al.*[50] for oxide ion diffusion in β-$La_2Mo_2O_9$ using ^{18}O tracer experiments above 570 °C.

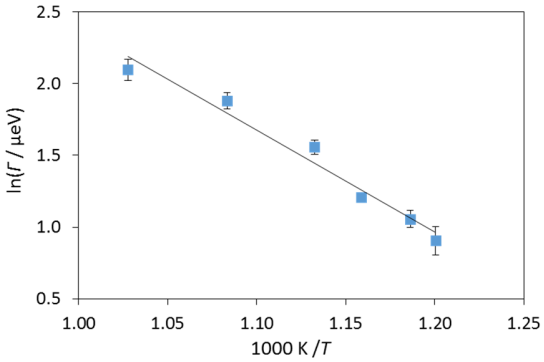

Figure 6. An Arrhenius plot showing the variation of the spectral linewidth with inverse temperature for QENS signals for $La_2Mo_2O_9$ over a 560-700 °C temperature range. The linewidths were determined by least squares fitting and the error bars represent the uncertainties from these fits.

Both these activation energies are lower than the value of 1.2 eV found for β-$La_2Mo_2O_9$ by Lacorre *et al.*[1] using impedance spectroscopy. Differences between activation energies determined from macroscopic measurements such as impedance spectroscopy and microscopic measurements such as neutron scattering or NMR have previously been reported for oxide ion conductors[51, 52], Na^+ conductors[53-55] and Li^+ conductors.[56, 57] In the present case it was also found that the microscopic measurements give significantly lower activation energies. This is presumably related to grain boundary or pellet density effects in impedance measurements leading to higher values, whereas the direct observation of dynamics using neutron scattering techniques have no (or minimal) dependence on sample morphology or form.

The Q-dependence of the QENS signal was also analysed using the Chudley-Elliott model (figure S2).[49] The values for the jump distance, l, and lifetime, τ, obtained are 2.98 Å and 1.8 ns, respectively. The lifetime found is in good agreement with the relaxation time reported by Kezionis *et al.*[32] for the process occurring at higher temperatures (to which they refer to as the β-process, equivalent to our process involving O1 atoms, *vide infra*).

Conduction Mechanisms Investigated by Ab Initio Molecular Dynamics

AIMD simulations were performed at four temperatures, with the 500°C representing a baseline with which we compared the dynamics at elevated temperatures, when the material becomes an excellent ionic conductor. Figure 7a shows the mean square displacement (MSD) of the oxygen atoms at each temperature for the first 100 ps calculated. As expected, the MSDs grow larger as temperature increases indicating increased oxide ion mobility. There is no evidence of the MSD saturating at any of the temperatures studied, indicating that the motion is not confined to a fixed volume.

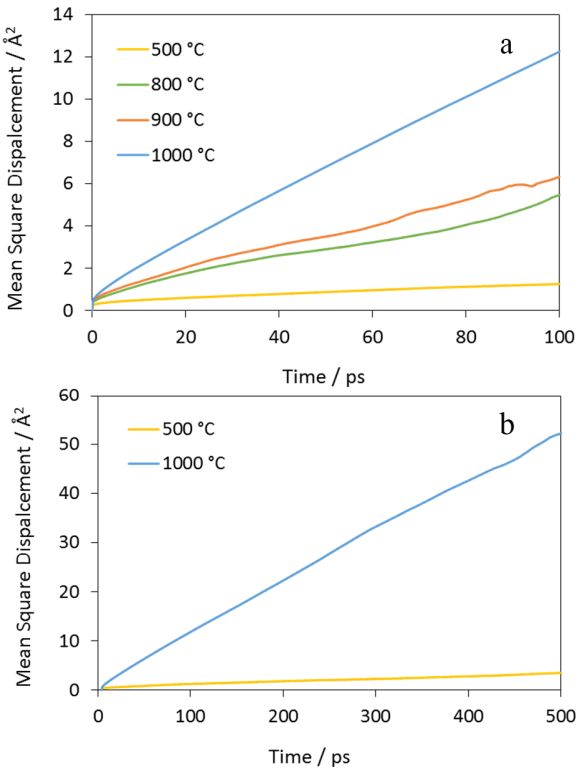

Figure 7. a) Mean square displacements for oxygen atoms calculated from trajectories of 100 ps from AIMD simulations at several temperatures. **b)** MSDs for oxygen atoms over the entire simulation at 1000 °C and 500 °C

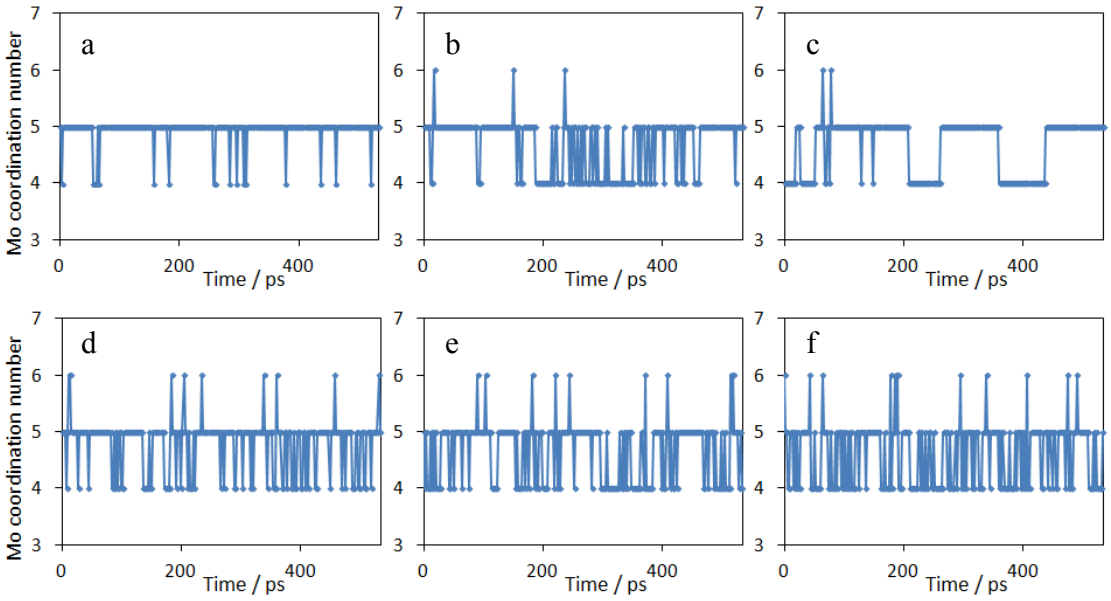

Figure 8: Variation of the coordination numbers of three Mo atoms over the course of the simulation. The top three are at 500 °C and the bottom three are at 1000 °C. The same three Mo atoms were chosen at each temperature represented by a/d; b/e; and c/f.

This is in contrast to the MSDs reported by Hou *et al.*[31], who found saturation at temperatures up to 927 °C, possibly due to the small simulation box they used providing poor sampling of diffusion events at intermediate temperature. In our simulations, apart from at the lowest temperature simulated, the average displacement is above 2.2 Å, i.e. longer than the shortest distance between different oxygen sites on the disordered MoO_x polyhedra (figure 1), indicating that substantial oxide ion migration between different Mo sites is occurring. Figure 7b shows the MSDs at 500 °C and 1000 °C over the full length of the simulations carried out at these temperatures. The 500 °C MSD gives a final average displacement over 500 ps of ≈ 1.9 Å, larger than the shortest distance between potential O sites on the same MoO_x polyhedron, but smaller than the shortest O-O distance between two adjacent MoO_x polyhedra. This means that some jumping between sites is occurring, albeit at a significantly lower rate than at the higher temperature; in this sense the 500 °C simulation, based on a cubic cell different from the average structure at this temperature but consistent with the local structure (as explained in the Experimental), is used only as a baseline with which to compare the results of the simulations at higher temperature, and not as a model for the dynamics of the monoclinic form stable at this temperature. The 1000 °C MSD continues to grow with time without saturation reaching an average displacement of ≈ 7.1 Å, almost equivalent to the length of a β-$La_2Mo_2O_9$ unit cell edge, indicating significant long-range oxide ion diffusion.

In order to compare the number of diffusion events occurring at 500 °C and 1000 °C, the oxide ion jumps that occurred during each trajectory were counted. For this purpose, a jump was defined as an oxide ion moving a distance of at least 1.5 Å (the smallest distance between partially occupied crystallographic sites shown in figure 1) within 500 simulations steps, and it was noted whether the closest Mo atom was the same or different before and after the jump. On this basis, each jump was classified as an intra-MoO_x or an inter-MoO_x jump. Table 1 shows the numbers of jumps recorded at each temperature.

Table 1. The number of intra-MoO_x and inter-MoO_x oxide ion jumps counted over the entire simulation at 500 °C and 1000 °C. Percentages of each type are also shown.

Type of jump	500 °C		1000 °C	
	Count	%	Count	%
Intra-MoO_x	143	62	1113	60
Inter-MoO_x	88	38	755	40
Total	231	100	1868	100

At both temperatures approximately 60 % of the events were intra-MoO_x jumps, with the rest being inter-MoO_x jumps. This indicates that the overall oxide ion migration mechanisms in $La_2Mo_2O_9$ consists of two main processes: the movement of oxide ions from one site to a vacant site on the same Mo atom, which is a local motion, and jumping between different Mo atom sites, which accounts for the long-range motion. It is the ability of Mo^{6+} to support variable coordination environments that allows this long-range motion to occur. The average jump distance at both

temperatures is 1.8 ± 0.3 Å, which is slightly longer than the distance between nearest partially occupied crystallographic sites.

Plots of the evolution of the coordination number (defined here as the number of oxygen atoms within 2.5 Å, determined based on the pair distribution function obtained from the calculations) of each Mo atom throughout the simulations illustrate that Mo atoms change coordination number between 4, 5 and 6; this is demonstrated for three Mo atoms in figure 8. It should be noted that no Mo was observed becoming 3- or 7-coordinate, which indicates that an oxide ion can only jump from a 5- or 6-coordinate Mo to a 4- or 5-coordinate one. The ratio of 4:5:6 coordinate Mo polyhedra in the room-temperature monoclinic structure is 15:15:18, and the fact that oxide ions cannot diffuse away from a 4-coordinate Mo, enhances the intra-site diffusion at elevated temperatures. The ≈ 40 % proportion of inter-MoO_x jumps therefore represents significant long-range diffusion on a similar time-scale as intra-MoO_x motions.

Figures 10a and 10b compare the MSDs of the oxide ions that are initially located on each oxygen site shown in figure 6. At 1000 °C (figure 9b), the O1, O2 and O3 site oxide ions all undergo significant displacement, which indicates that all sites are involved in the long-range conduction process at high temperature. However, at 500 °C the MSD of the O atoms belonging initially to the O1 site saturates very quickly (figure 9a), with an average displacement of ≈ 1.4 Å, whereas the O2 and O3 show no sign of saturation. The distance of 1.4 Å is shorter than the distance between the O1 sites and O2/O3, indicating that the O1 ions at lower temperatures remain confined to their local site and do not contribute to conductivity.

The confinement of the O1 ions to their site is further confirmed by inspection of cloud plots showing the regions visited by oxygen atoms during the MD simulations. At 500 °C (figure 10a) the clouds for the O1 atoms remain around one site, and represent local thermal motion. In contrast, the O2 oxygen atoms move between the available vacant O2 and O3 sites surrounding a given Mo, i.e. undergo intra-MoO_x motion (figure 10b). While relatively less frequent, the O2 and O3 oxide ions can also be seen to undergo inter-MoO_x motion, i.e. exchange between different Mo atoms, as shown in figure 10c where an O2 from a 5-coordinate Mo moves to a vacant O3 site on an adjacent 4-coordinate Mo.

At 1000 °C the O1 atoms can leave their site and contribute to the overall conductivity (figure 10d). Corbel *et al.*[30], suggested that the O1 oxygens leave their site to jump directly to O2 and O3 sites on adjacent Mo atoms, a distance of approximately 2.8 Å. However, we found that O1 ions move to an O2 site within the same Mo coordination sphere first, and from there follow the same intra-MoO_x and inter-MoO_x jump mechanisms as O2 and O3 atoms.

The mechanisms we find are similar to those reported by Hou *et al.*[31] although the key difference is that they found two oxide ion migration processes occurring at all temperatures, one involving the O1 site and one without. Our findings indicate that the O1 sites are activated at higher temperatures than O2 and O3, providing extra charge carriers and vacancies initially allowing for increased intra-MoO_x motion of oxide ions, which then translates into increased long-range inter-MoO_x diffusion.

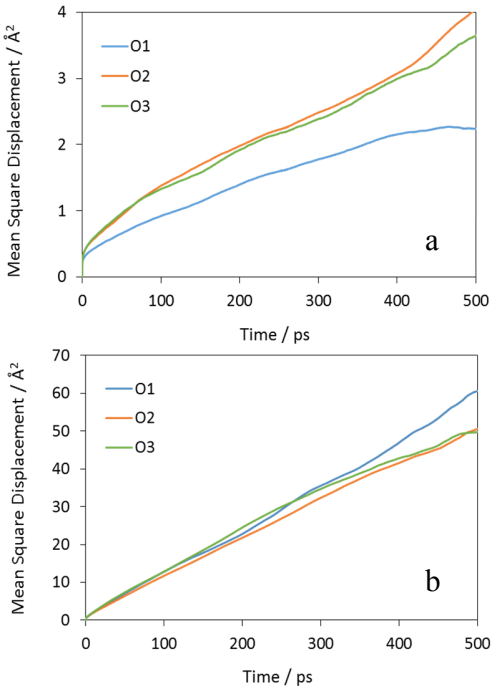

Figure 9: a) Mean square displacements for oxide ions initially located in each of the three oxygen sites during the simulation at 500 °C. **b)** MSDs for oxide ions initially located in each of the three sites during the simulation at 1000 °C. Note that the y-axis scale is around 10× larger in **b)** than **a).**

This activation of O1 at higher temperatures agrees well with the recent experimental observations by Kezionis *et al.*[32] They find two processes leading to the bulk conductivity in $La_2Mo_2O_9$, one below the phase transition (and persisting above it), equivalent to our low temperature process involving O2 and O3, and one which appears above the phase transition, equivalent to our high temperature process involving O1. Our findings also explain why the low-temperature process could still be observed at higher temperatures, as this process still remains as a significant part of the overall conductivity mechanism. The nanosecond order relaxation times they report for the high temperature process coincide with the timescales observable by IN16b and agree well with our Chudley-Elliott fitting of the QENS data. Our simulations show that the high temperature process involves O1 sites with longer jump distances, which may provide an explanation for the relatively large (2.98 Å) jump distance found in the fit if it is this motion that is "seen" by IN16b.

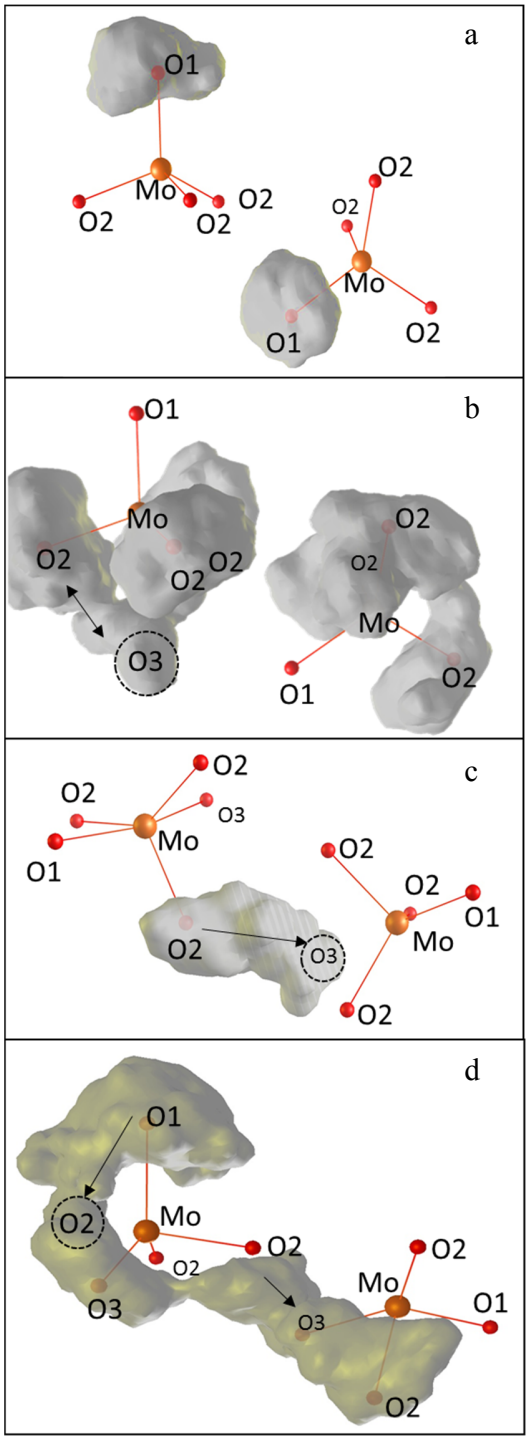

Figure 10. Representative cloud plots showing the space visited by oxide ions during the course of the AIMD simulations. **a)** O1 atoms undergoing localised thermal motion during simulation at 500 °C. **b)** O2 atoms undergoing intra-MoO_x motion to an O3 site during the same simulation. **c)** A cloud showing an inter-MoO_x jump between two adjacent Mo atoms at 500 °C. **d)** Long-range motion of an O1 ion during the course of the simulation at 1000 °C.

Conclusions

In this work, quasielastic and inelastic neutron scattering measurements have been combined with AIMD simulations to directly observe and provide atomic-level understanding of the oxide ion dynamics on the nanosecond time-scale in the solid electrolyte $La_2Mo_2O_9$.

We have demonstrated the successful use of the easily accessible laboratory based VTXRD data as a screening method for potential neutron scattering experiments. The QENS measurements suggest that oxide ion diffusion in $La_2Mo_2O_9$ occurs on nanosecond timescales. The activation energy determined from the QENS measurements, 0.61(5) eV, is consistent with the values obtained from other techniques. These results represent observation of oxygen dynamics by neutron scattering on the longest timescales reported to date. The fitting of the Q dependence of the QENS signal provides a conductivity timescale that agrees with macroscopic measurements, further reinforcing the link between the micro and macroscopic processes.

The AIMD simulations reveal that a combination of variable coordination number of Mo and the ease of movement of oxide ions within an MoO_x coordination sphere ultimately leads to the high long-range conduction observed in $La_2Mo_2O_9$. At low temperatures, the dominant process is the intra-MoO_x exchange between the O2 and O3 sites, although some inter-MoO_x motion occurs; the O1 oxygens are confined to their sites and not involved in the conduction process. At higher temperatures the O1 sites become involved and the oxide ions become free to move from O1 to the partially occupied O2 and O3 sites to contribute to the overall conduction mechanism. Long-range diffusion then proceeds via the exchange of oxide ions in O2 and O3 sites in one Mo coordination sphere with O3 and O2 sites on adjacent Mo atoms, assisted by intra-MoO_x jumps within each coordination sphere. While intra- and inter-site jumps can be distinguished in the simulations, they occur on similar time- and length-scales of several nanoseconds and Angströms respectively, which is characteristic of a uniform diffusion process. The time and length scales obtained from AIMD simulations are consistent with those obtained from QENS experiments and provide an explanation for values found from Chudley Elliott fitting.

This represents the first atomic-level understanding of the oxide ion dynamics in $La_2Mo_2O_9$ which is consistent with the experimental observations on this material.

ASSOCIATED CONTENT

Supporting Information containing the unit cell parameters dependence on temperature and the details of the fitting of the scattering functions is available. This material is available free of charge via the Internet at http://pubs.acs.org.

AUTHOR INFORMATION

Corresponding Author

*ivana.radosavljevic@durham.ac.uk

Funding Sources

The authors thank Durham University and Institut Laue Langevin for a PhD studentship for J. R. P. and Institut Laue Langevin for a summer research studentship for C. A. F.

References

1. Lacorre, P.; Goutenoire, F.; Bohnke, O.; Retoux, R.; Laligant, Y., Designing fast oxide-ion conductors based on La2Mo2O9. *Nature* **2000,** 404, 856-858.
2. Goutenoire, F.; Isnard, O.; Retoux, R.; Lacorre, P., Crystal structure of La2Mo2O9, a new fast oxide-ion conductor. *Chem. Mater.* **2000,** 12, 2575-2580.
3. Georges, S.; Goutenoire, F.; Altorfer, F.; Sheptyakov, D.; Fauth, F.; Suard, E.; Lacorre, P., Thermal, structural and transport properties of the fast oxide-ion conductors La2-xRxMo2O9 (R=Nd, Gd, Y). *Solid State Ionics* **2003,** 161, 231-241.
4. Evans, I. R.; Howard, J. A. K.; Evans, J. S. O., The crystal structure of alpha-La2Mo2O9 and the structural origin of the oxide ion migration pathway. *Chem. Mater.* **2005,** 17, 4074-4077.
5. Malavasi, L.; Kim, H.; Billinge, S. J. L.; Proffen, T.; Tealdi, C.; Flor, G., Nature of the monoclinic to cubic phase transition in the fast oxygen ion conductor La2Mo2O9 (LAMOX). *J. Am. Chem. Soc.* **2007,** 129, 6903-6907.
6. Fang, Q. F.; Wang, X. P.; Zhang, G. G.; Yi, Z. G., Damping mechanism in the novel La2Mo2O9-based oxide-ion conductors. *J. Alloys Compd.* **2003,** 355, 177-182.
7. Wang, X. P.; Cheng, Z. J.; Fang, Q. F., Influence of potassium doping on the oxygen-ion diffusion and ionic conduction in the La2Mo2O9 oxide-ion conductors. *Solid State Ionics* **2005,** 176, 761-765.
8. Tealdi, C.; Chiodelli, G.; Malavasi, L.; Flor, G., Effect of alkaline-doping on the properties of La2Mo2O9 fast oxygen ion conductor. *J. Mater. Chem.* **2004,** 14, 3553-3557.
9. Goutenoire, F.; Isnard, O.; Suard, E.; Bohnke, O.; Laligant, Y.; Retoux, R.; Lacorre, P., Structural and transport characteristics of the LAMOX family of fast oxide-ion conductors, based on lanthanum molybdenum oxide La2Mo2O9. *J. Mater. Chem.* **2001,** 11, 119-124.
10. Tian, C. A.; Yin, Q. Y.; Xie, J. S.; Yang, J.; Sun, H.; Ji, B. F.; Bao, W. T., Chemical synthesis and properties of La1.9Ba0.1Mo1.9Mn0.1O9 as electrolyte for IT-SOFCs. *Journal of Rare Earths* **2014,** 32, 423-428.
11. Paul, T.; Ghosh, A., Correlation of structure and ion conduction in La2-xYxMo2O9 oxygen ion conductors. *J. Appl. Phys.* **2015,** 117.
12. Corbel, G.; Durand, P.; Lacorre, P., Comprehensive survey of Nd3+ substitution In La2Mo2O9 oxide-ion conductor. *J. Solid State Chem.* **2009,** 182, 1009-1016.
13. Marrero-Lopez, D.; Canales-Vazquez, J.; Zhou, W. Z.; Irvine, J. T. S.; Nunez, P., Structural studies on W6+ and Nd3+ substituted La2Mo2O9 materials. *J. Solid State Chem.* **2006,** 179, 278-288.
14. Paul, T.; Ghosh, A., Structural and electrical properties of Er doped La2Mo2O9 oxide ion conductors. *J. Appl. Phys.* **2016,** 119.
15. Corbel, G.; Chevereau, E.; Kodjikian, S.; Lacorre, P., Topological metastability and oxide ionic conduction in La2-xEuxMo2O9. *Inorg. Chem.* **2007,** 46, 6395-6404.
16. Jin, T. Y.; Rao, M. V. M.; Cheng, C. L.; Tsai, D. S.; Hung, M. H., Structural stability and ion conductivity of the Dy and W substituted La2Mo2O9. *Solid State Ionics* **2007,** 178, 367-374.
17. Liu, X.; Fan, H. Q.; Shi, J.; Dong, G. Z.; Li, Q., High oxide ion conducting solid electrolytes of bismuth and niobium co-substituted La2Mo2O9. *Int. J. Hydrogen Energy* **2014,** 39, 17819-17827.
18. Alekseeva, O. A.; Verin, I. A.; Sorokina, N. I.; Krasil'nikova, A. E.; Voronkova, V. I., Crystal Structure of La2Mo2O9 Single Crystals Doped with Bismuth. *Crystallography Reports* **2010,** 55, 583-590.
19. Wang, X. P.; Fang, Q. F.; Li, Z. S.; Zhang, G. G.; Yi, Z. G., Dielectric relaxation studies of Bi-doping effects on the oxygen-ion diffusion in La2-xBixMo2O9 oxide-ion conductors. *Appl. Phys. Lett.* **2002,** 81, 3434-3436.
20. Takai, S.; Doi, Y.; Torii, S.; Zhang, J. R.; Putra, T.; Miao, P.; Kamiyama, T.; Esaka, T., Structural and electrical properties of Pb-substituted La2Mo2O9 oxide ion conductors. *Solid State Ionics* **2013,** 238, 36-43.
21. Alekseeva, O. A.; Antipin, A. M.; Gagor, A.; Pietraszko, A.; Novikova, N. E.; Sorokina, N. I.; Kharitonova, E. P.; Voronkova, V. I., Single-crystal structure of vanadium-doped La2Mo2O9. *Crystallography Reports* **2013,** 58, 829-834.
22. Georges, S.; Bohnke, O.; Goutenoire, F.; Laligant, Y.; Fouletier, J.; Lacorre, P., Effects of tungsten substitution on the transport properties and mechanism of fast oxide-ion conduction in La2Mo2O9. *Solid State Ionics* **2006,** 177, 1715-1720.
23. Liu, W.; Pan, W.; Luo, J.; Godfrey, A.; Ou, G.; Wu, H.; Zhang, W., Suppressed phase transition and giant ionic conductivity in La2Mo2O9 nanowires. *Nature Communications* **2015,** 6.
24. Tealdi, C.; Chiodelli, G.; Flor, G.; Leonardi, S., Electrode stability and electrochemical performance of Lamox electrolytes under fuel cell conditions. *Solid State Ionics* **2010,** 181, 1456-1461.
25. Le, M. V.; Tsai, D. S.; Yao, C. C.; Lo, J. C.; Vo, T. P. G., Properties of 10% Dy-doped La2Mo2O9 and its electrolyte performance in single chamber solid oxide fuel cell. *J. Alloys Compd.* **2014,** 582, 780-785.
26. Ravella, U. K.; Liu, J. J.; Corbel, G.; Skinner, S. J.; Lacorre, P., Cationic Intermixing and Reactivity at the La2Mo2O9/La0.8Sr0.2MnO3- Solid Oxide Fuel Cell Electrolyte-Cathode Interface. *ChemSusChem* **2016,** 9, 2182-2192.
27. Goel, M.; Djurado, E.; Georges, S., Reducibility of La2Mo2O9 based ceramics versus porosity. *Solid State Ionics* **2011,** 204, 97-103.
28. Buvat, G.; Sellemi, H.; Ravella, U.; Barre, M.; Coste, S.; Corbel, G.; Lacorre, P., Reduction kinetics of La2Mo2O9 and phase evolution during reduction and reoxidation. *Inorganic Chemistry* **2016,** 55, 2522-2533.
29. Buvat, G.; Quarez, E.; Joubert, O., Innovative solid oxide fuel cells based on Ba1no.3Ti0.7O2.85 electrolyte and La2Mo2O9 amorphous reduced phase as anode material. *J. Power Sources* **2016,** 302, 107-113.
30. Corbel, G.; Suard, E.; Lacorre, P., Structural Key of the Thermal Expansion and the Oxide Ionic Conduction in Derivatives of La2Mo2O9: a Temperature-Controlled Neutron Diffraction Study of β-La1.7Bi0.3Mo2O9. *Chem. Mater.* **2011,** 23, 1288-1298.
31. Hou, C. J.; Li, Y. D.; Wang, P. J.; Liu, C. S.; Wang, X. P.; Fang, Q. F.; Sun, D. Y., Oxygen-ion arrangements and concerted motion in beta-La2Mo2O9. *Physical Review B* **2007,** 76.
32. Kezionis, A.; Petrulionis, D.; Kazakevicius, E.; Kazlauskas, S.; Zalga, A.; Juskenas, R., Charge carrier relaxation phenomena and phase transition in La2Mo2O9 ceramics investigated by broadband impedance spectroscopy. *Electrochim. Acta* **2016,** 213, 306-313.
33. Hempelmann, R., *Quasielastic neutron scattering and solid state diffusion*. Oxford University Press: New York, 2000; p 304.
34. Hempelmann, R., Diffusion of hydrogen in metals. *Journal of the Less Common Metals* **1984,** 101, 69-96.
35. Kim, H. J.; Magerl, A.; Fischer, J. E.; Vaknin, D.; Heitjans, P.; Schirmer, A., Li diffusion in stage 2 Li-graphite intercalation compounds studied with quasielastic neutron scattering. In *Chemical Physics of Intercalation II*, Bernier, P.; Fischer, J. E.; Roth, S.; Solin, S. A., Eds. Springer US: Boston, MA, 1993; pp 355-359.
36. Karlsson, M., Proton dynamics in oxides: insight into the mechanics of proton conduction from quasielastic neutron scattering. *PCCP* **2015,** 17, 26-38.

37. Catlow, C. R. A., Atomistic mechanisms of ionic transport in fast-ion conductors. *J. Chem. Soc., Faraday Trans.* **1990,** 86, 1167-1176.
38. Ling, C. D.; Miiler, W.; Johnson, M. R.; Richard, D.; Rols, S.; Madge, J.; Evans, I. R., Local Structure, Dynamics, and the Mechanisms of Oxide Ionic Conduction in Bi26Mo10O69. *Chem. Mater.* **2012,** 24, 4607-4614.
39. Auckett, J. E.; Studer, A. J.; Pellegrini, E.; Ollivier, J.; Johnson, M. R.; Schober, H.; Miiller, W.; Ling, C. D., Combined Experimental and Computational Study of Oxide Ion Conduction Dynamics in Sr2Fe2O5 Brownmillerite. *Chem. Mater.* **2013,** 25, 3080-3087.
40. Mamontov, E., Fast oxygen diffusion in bismuth oxide probed by quasielastic neutron scattering. *Solid State Ionics* **2016,** 296, 158-162.
41. Jalarvo, N.; Gourdon, O.; Bi, Z.; Gout, D.; Ohl, M.; Paranthaman, M. P., Atomic-scale picture of the ion conduction mechanism in a tetrahedral network of lanthanum barium gallate. *Chem. Mater.* **2013,** 25, 2741-2748.
42. Rietveld, H. M., A Profile Refinement Method for Nuclear and Magnetic Structures. *J. Appl. Cryst.* **1969,** 2, 65-71.
43. Coelho, A. A.; Evans, J. S. O.; Evans, I. R.; Kern, A.; Parsons, S., The TOPAS symbolic computation system. *Powder Diffr.* **2011,** 26, S22-S25.
44. Richard, D.; Ferrand, M.; G.; Kearley, J., LAMP. *Journal of Neutron Research* **1996,** 4, 33-39.
45. Kresse, G.; Furthmuller, J., Efficiency of ab-initio total energy calculations for metals and semiconductors using a plane-wave basis set. *Computational Materials Science* **1996,** 6, 15-50.
46. Kresse, G.; Joubert, D., From ultrasoft pseudopotentials to the projector augmented-wave method. *Physical Review B* **1999,** 59, 1758-1775.
47. Perdew, J.; Burke, K.; Ernzerhof, M., Generalized gradient approximation made simple. *Phys. Rev. Lett.* **1996,** 77, 3865-3868.
48. Pellegrini, E. C.; Goret, G.; Aoun, A., MDANSE a versatile application for analysing molecular dynamics data. **2016**.
49. Chudley, C. T.; Elliott, R. J., Neutron Scattering from a Liquid on a Jump Diffusion Model. *Proceedings of the Physical Society of London* **1961,** 77, 353-&.
50. Liu, J.; Chater, R. J.; Hagenhoff, B.; Morris, R. J. H.; Skinner, S. J., Surface enhancement of oxygen exchange and diffusion in the ionic conductor La2Mo2O9. *Solid State Ionics* **2010,** 181, 812-818.
51. Kim, N.; Hsieh, C.; Huang, H.; Prinz, F.; Stebbins, J., High temperature O-17 MAS NMR study scandia and yttria stabilized of calcia, magnesia, zirconia. *Solid State Ionics* **2007,** 178, 1499-1506.
52. Fuda, K.; Kishio, K.; Yamauchi, S.; Fueki, K.; Onoda, Y., O17 NMR-Study of Y_2O_3-doped CeO_2. *J. Phys. Chem. Solids* **1984,** 45, 1253-1257.
53. Peet, J. R.; Widdifield, C. M.; Apperley, D. C.; Hodgkinson, P.; Johnson, M. R.; Evans, I. R., Na+ mobility in sodium strontium silicate fast ion conductors. *Chem. Commun.* **2015,** 51, 17163-17165.
54. Yamada, K.; Kumano, K.; Okuda, T., Conduction path of the sodium ion in Na3InCl6 studied by X-ray diffraction and Na-23 and In-115 NMR. *Solid State Ionics* **2005,** 176, 823-829.
55. Udovic, T.; Matsuo, M.; Tang, W.; Wu, H.; Stavila, V.; Soloninin, A.; Skoryunov, R.; Babanova, O.; Skripov, A.; Rush, J.; Unemoto, A.; Takamura, H.; Orimo, S., Exceptional Superionic Conductivity in Disordered Sodium Decahydro-closo-decaborate. *Adv. Mater.* **2014,** 26, 7622-7626.
56. Santibáñez-Mendieta, A. B.; Didier, C.; Inglis, K. K.; Corkett, A. J.; Pitcher, M. J.; Zanella, M.; Shin, J. F.; Daniels, L. M.; Rakhmatullin, A.; Li, M.; Dyer, M. S.; Claridge, J. B.; Blanc, F.; Rosseinsky, M. J., La3Li3W2O12: Ionic Diffusion in a Perovskite with Lithium on both A- and B-Sites. *Chem. Mater.* **2016,** 28, 7833-7851.
57. Arbi, K.; Lazarraga, M.; Chehimi, D.; Ayadi-Trabelsi, M.; Rojo, J.; Sanz, J., Lithium mobility in Li1.2Ti1.8Ro.2(PO4)(3) compounds (R = Al, Ga, Sc, In) as followed by NMR and impedance spectroscopy. *Chem. Mater.* **2004,** 16, 255-262.